Comparing the plasmonic properties of laser and chemically synthesized SeNPs for localized surface plasmon resonance detection

Journal of Physics: Photonics

PAPER

Comparing the plasmonic properties of laser and chemically synthesized SeNPs for localized surface plasmon resonance detection

Z K S Mcotshana[1,2], L N Thwala[1,*], S Ombinda-Lemboumba[1], R Ramokolo[1], M Sekhwama[1,3], S L Thobakgale[1], M Y Lugongolo[1], L Hlekelele[4], K T Mpofu[1], E Van Steen[2] and P Mthunzi-Kufa[5]

[1] National Laser Centre, Council for Scientific and Industrial Research, PO Box 395, Pretoria 0001, South Africa
[2] Department of Chemical Engineering, University of Cape Town, Private Bag X3, Rondebosch, Cape Town 7700, South Africa
[3] Division of Biomedical Engineering, Department of Human Biology, University of Cape Town, Private Bag X3, Rondebosch, Cape Town 7700, South Africa
[4] Centre for Nanostructures and Advanced Materials DSI-CSIR Nanotechnology Innovation Centre Council for Scientific and Industrial Research, Pretoria 0001, South Africa
[5] School of Science, College of Science, Engineering and Technology, University of South Africa, Private Bag X90, Florida 1710, South Africa
[*] Author to whom any correspondence should be addressed.

E-mail: LThwala@csir.co.za

Keywords: selenium nanoparticles, SARS-CoV-2, localized surface plasmon resonance, photonics, biosensing

OPEN ACCESS

RECEIVED
19 June 2025

REVISED
13 August 2025

ACCEPTED FOR PUBLICATION
28 August 2025

PUBLISHED
11 September 2025

Abstract

Localized surface plasmon resonance (LSPR) sensing offers a rapid, label-free, and highly sensitive approach for detecting biomolecular interactions. This study investigates the LSPR characteristics of selenium (Se) nanoparticles (NPs) synthesized via two distinct approaches: pulsed laser ablation in liquid and chemical reduction, for the development of an optical sensor to detect Severe Acute Respiratory Syndrome Coronavirus 2 (SARS-CoV-2). The laser ablation method produced ligand-free Se NPs with high purity and narrow size distribution, while the chemical reduction route yielded NPs with tunable morphology and surface functionalization capability. The selenium NPs (SeNPs) were characterized by ultraviolet–visible spectroscopy, dynamic light scattering, and high-resolution transmission electron microscopy. Raman spectroscopy was used to determine the functional groups on the surfaces of SeNPs. Thereafter, an optical biosensing substrate pre-coated with 3-aminopropyltriethoxysilane was functionalized with the SeNPs and conjugated with SARS-CoV-2 monoclonal antibodies to offer specificity for SARS-CoV-2. After characterization, the biosensing substrate was used for detecting SARS-CoV-2 pseudovirus (analyte) using LSPR. In the presence of SARS-CoV-2, the local refractive index around the SeNPs functionalized with the antibody increased, leading to a red shift in the LSPR peak when compared to the control sample. Furthermore, when the antibody captured the SARS-CoV-2 antigen, the SeNPs synthesized by the chemical reduction approach (C-SeNPs) exhibited a higher redshift compared to laser-synthesized SeNPs, indicating that C-SeNPs are good candidates for biosensing applications in optical techniques. The difference in LSPR shifts between the two types of NPs reflects their unique sensitivity to biomolecular interactions. These findings demonstrate that synthesis method selection influences LSPR sensor performance, and highlight the potential of Se NPs, particularly those prepared by the chemical reduction method, as promising plasmonic transducers for fast and cost-effective COVID-19 diagnostics.

1. Introduction

Despite significant advances in diagnostic technologies, the global spread of viral infectious diseases such as Severe Acute Respiratory Syndrome Coronavirus 2 (SARS-CoV-2) continues to pose a major public health challenge [1]. The most widely used, highly effective, and approved technologies for viral pathogen screening

and diagnosis are reverse transcription loop-mediated isothermal amplification and polymerase chain reaction, among others. These methods, which use ribonucleic acid as a starting material for nucleic acid amplification, are sensitive and are considered the gold standard [2–4]. However, these diagnostic tools have proven challenging; they are laboratory-based, requiring high-tech equipment, and multiple other diagnostic techniques must be performed to provide a precise diagnosis, which could result in a lengthy wait for the patient [4, 5]. It is necessary to develop and enhance the present diagnostic tools into effective, sensitive diagnostic tools that are accessible at the point-of-care (POC) setting, to detect infectious viruses such as SARS-CoV-2.

The field of optical techniques has improved to be used as a testing procedure for different viral diseases. Credit is due to recent research involving optical sensors that can be produced as POC diagnostic tools, such as surface-enhanced Raman scattering, and localized surface plasmon resonance (LSPR) [6]. Optical techniques, such as LSPR, have the potential to be a key tool in disease diagnosis because of their rapid, sensitive, easy-to-use, and economical methods [7]. LSPR is a method in which electromagnetic radiation interacts with a metal nanoparticle (NP) to induce coherent excitations in the conduction electrons [8]. This interaction produces oscillations of LSPs with a resonance frequency, which is closely linked to the refractive index (RI) of the environment surrounding NPs. The RI is influenced by surface characteristics such as the size, shape, interparticle distance, and composition of the NPs [9, 10]. When the size of a particle is smaller than the incident light's wavelength, the light is absorbed by the electron density, thus displacing the electrons from their usual position, resulting in polarization or separation of charges. The electrostatic forces between the electron cloud and positive ions bring about a restoring force that permits electron oscillation with a specific frequency known as the particle dipole plasmon frequency. Both the restoring force and the absorption of electromagnetic radiation reach their maximum at the resonance frequency [11].

The LSPR technique is effective because of the high conductivity and capacity of metallic NPs (MNPs) to sustain strong plasmonic resonances [12]. In addition, MNPs are promising agents due to their advantageous optical characteristics, including scattering properties [13], biocompatibility [14], and well-established bioconjugation techniques [15]. There are various methods used to synthesize MNPs, including chemical reduction and laser ablation. Each method has advantages and distinct properties. For example, the chemical reduction method often produces small-sized NPs. The size and shape of the NPs are dependent on the selection of the stabilizer, reducing agent, and reaction conditions, which can prevent NPs from aggregating [16–18]. The laser ablation method has the advantage of producing pure NPs because it requires no additional reagents but deionized water to produce the particles [19]. In addition, this method is eco-friendly and efficient [20].

Selenium NPs (SeNPs) have garnered significant attention in medical diagnostics and treatments, due to their low toxicity and biocompatibility [21]. However, in photonic diagnostics, SeNPs have not yet been fully investigated. The interest in SeNPs is expanding because of a better understanding of their exceptional plasmonic properties; hence, the need to explore them in this study. SeNPs have light-absorbing capabilities, are stable, and are easy to manufacture [22–24]. These properties make them potentially appropriate for use as signal enhancers in the biosensing field [25, 26].

The need to improve existing diagnostics, such as photonic approaches using NPs, and further develop them into effective diagnostic instruments is advancing. There are exciting prospects for the development of biosensing capabilities with photonic-based diagnostic instruments composed of MNPs, which can provide rapid, sensitive, and accurate results [19, 27]. Kunwar *et al* [28] demonstrated that the use of hybrid silver–gold (AgAu) alloy NPs in UV photodetectors enhances the sensor's photoresponse through plasmonic absorption [28]. Bigdeli *et al* [29] and Li *et al* [30] reported that the conventional SPR sensor, which uses a flat metal–dielectric interface, such as gold or silver, achieved ultrahigh sensitivity in the presence of NPs compared to when NPs were on a dielectric substrate [29, 30]. This enhancement was accomplished by using the Kretschmann–Raether configuration, which excites the LSPs through extended surface plasmons generated at the metallic film surface [30]. Furthermore, Stewart *et al* [31] attested that increased RI and larger SPR shifts resulted from the incorporation of metal NPs onto the SPR metal surface [31].

Anker *et al* [32] stated that the combination of hybrid NPs has significantly increased optical sensor sensitivity and has been used extensively in RI sensing. The authors reported on the LSPR sensor, explaining how the morphology of NPs can contribute to the sensor's sensitivity, and further utilized it to detect molecular binding events [32].

A LSPR sensor that uses plasmonic SeNPs as signal enhancers for the detection of SARS-CoV-2 pseudovirus is proposed in this investigation. A biosensing glass substrate was prepared and functionalized with SeNPs that were synthesized using the chemical reduction and laser ablation methods. Thereafter, SeNPs were conjugated with SARS-CoV-2 monoclonal antibodies (SARS-CoV-2 mAbs) specific to SARS-CoV-2 pseudovirus. The biosensing substrate was then used to detect SARS-CoV-2 pseudovirus

utilizing an in-house-built LSPR set-up. The plasmonic effect of the two types of SeNPs on the LSPR was compared to determine whether the synthesis method used had a different impact on the LSPR signal.

2. Materials and methods

2.1. Materials

Selenium powder, 325-mesh, 99.5% (metals basis), and sodium selenite were purchased from Labchem, South Africa. SARS-CoV-2 Spike Antibody, Mouse Mab (40591-MM41) was purchased from Sino Biological, INC., China. N-hydroxysuccinimide (NHS), 3-aminopropyltriethoxysilane (APTES), and 1-ethyl-3-(3-dimethylaminopropyl) carbodiimide (EDC) were all purchased from Sigma-Aldrich, South Africa. Milli-Q grade (resistivity 18.2 MΩ cm^{-1}) water was used in all experiments.

2.2. Synthesis of SeNPs by laser ablation

2.2.1. Selenium pellet preparation

A commercial powder of metallic selenium, containing 99.5% (metal basis) that passes through a 325-mesh screen (∼44 μm), was pressed under a pressure of 5 tons using a Hydraulic pellet press machine to produce a selenium pellet having a thickness of 2.2 mm and a diameter of 14 mm. In this experiment, the pellet was sintered at 210 °C for about 5 min, i.e. below the melting point (221 °C) of metallic selenium.

2.2.2. Laser ablation setup and synthesis of SeNPs

The experimental setup for generating SeNPs by the laser ablation method is illustrated in figure 1. A collimated pulsed Nd:YAG laser with a 1064 nm wavelength was used in this study. The laser's power density was approximately ∼10^6 W cm^{-2} with a pulse duration of 10 ns. A 230 mm focal length spherical lens with a divergence angle of 0.0430 was used to focus the laser beam, resulting in a spot size of approximately 31 μm on the target. The selenium pellet (1.5 g) was dispersed into 35 ml of deionized water contained in a 100 ml glass beaker (Borosil glass). The pellet was irradiated with the 1064 nm Nd:YAG pulse laser at a 30 Hz repetition rate for 10 min, initiating the breakdown process that resulted in plasma formation due to the liquid environment. This process led to the expansion of a cavitation bubble, which eventually burst at its maximum radius [33]. Thereafter, the SeNPs were generated and released into the liquid, appearing orange in color.

2.3. Synthesis of SeNPs by chemical reduction method

SeNPs were also synthesized using the chemical reduction method. Briefly, sodium selenite was used as the precursor, ascorbic acid as the reducing agent, and cetyltrimethylammonium chloride (CTAC) was used as a stabilizer. About 0.2 M CTAC (1.25 ml) was added to 0.07 M ascorbic acid (20 ml) and stirred continuously using a magnetic stirrer at room temperature for 5 mins. Subsequently, 0.25 M sodium selenite was added to the mixture dropwise until the color changed from colorless to orange, confirming the formation of SeNPs [34]. The schematic representation of SeNPs synthesis is given in figure 2.

2.4. Characterization of SeNPs

The obtained NPs were characterized for their ultraviolet–visible (UV–Vis) absorption spectrum, using a NanoDrop 8000 UV–Vis spectrophotometer. Approximately 20 μl of the liquid sample was placed onto the measurement pedestal for analysis.

The Malvern Zetasizer Nano ZS (Malvern Instruments Ltd., United Kingdom) was utilized for dynamic light scattering (DLS) analysis; to determine the size distribution and surface charge of SeNPs, the samples used for DLS analysis were diluted 10x in milliQ water and analyzed in triplicate ($n = 3$).

High-resolution transmission electron microscopy (HR-TEM) images of SeNPs were acquired using a JEOL JEM-2100 HR-TEM. A drop of the sample was deposited on a 300-mesh carbon-coated copper grid and air-dried before being examined under HR-TEM at different magnifications.

Raman analysis was used to study chemical bonding and intramolecular bonds in the samples using a Horiba LabRam Soleil Raman microscope, with the following parameters: 532 nm laser wavelength, 7 mW laser power, 10x objective, 200 μm slid width, 20 scans, and 5 s per scan. Background subtraction and smoothing were performed using LabSpec 6 software, and a spectral region of 200–1000 cm^{-1} was chosen for qualitative analysis of the two methods used to prepare the NPs.

Furthermore, the techniques mentioned were used to study the effect that the SARS-CoV-2 mAb conjugate had on the absorbance, morphology, and surface charge of SeNPs.

2.5. Functionalization of SeNPs-mAb conjugate on LSPR glass substrate (biosensor chip)

The biosensor substrate (biosensor chip) was prepared by functionalizing a glass slide with SeNPs conjugated to SARS-CoV-2 mAb. Herein, a glass slide (Lasec, RSA) with [76 mm (L) × 26 mm (W) × 1 mm (H)] was

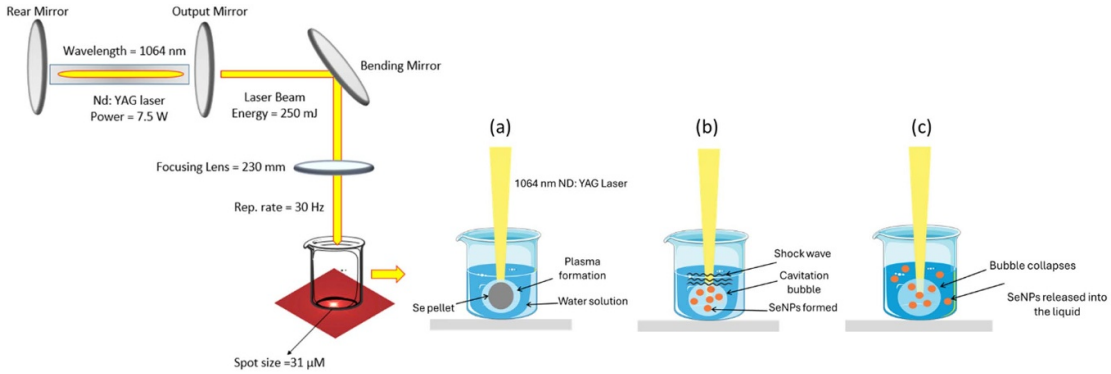

Figure 1. Schematic diagram of the laser ablation experimental setup for synthesizing selenium nanoparticles irradiated with 1064 nm pulsed Nd:YAG laser at 30 Hz. The process of laser ablation in liquid: (a) formation of plasma, (b) cavitation bubble formation and the generation of selenium nanoparticles (SeNPs), and (c) the release of SeNPs into the liquid.

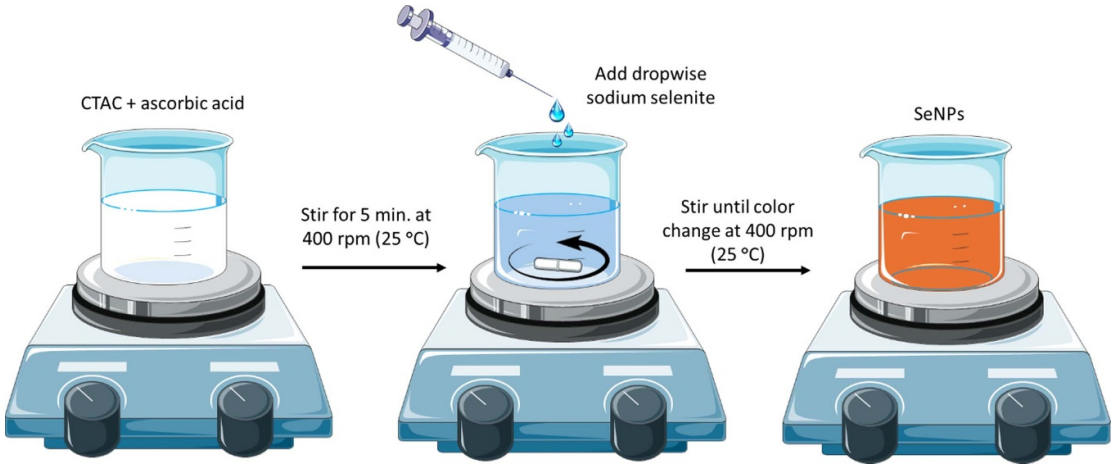

Figure 2. Schematic representation of the synthesis of SeNPs by the chemical reduction method.

treated with oxygen (O_2) plasma to create a hydrophilic surface (see figure 3(a)) and silanized with a coupling agent, 1% 3-aminopropyltriethoxysilane (APTES) for 30 min to generate a self-assembly monolayer (SAM) on the hydrophilic surface (figure 3(b)). Siloxane bonds are formed with hydroxyl groups on the glass substrate by the SAM employing APTES, which comprises head groups with Si and functional groups with amine. For negatively charged SeNPs produced by laser ablation (L-SeNPs), amine groups were protonated to (NH_3^+) with acidic buffer solution by creating a positively charged surface for binding the negatively charged NPs (figure 3(c)). For positively charged SeNPs produced by the chemical reduction method (C-SeNPs), the amine group (NH_2) was bound to the positively charged SeNPs. The NPs (20 μl) were incubated for 30 min to ensure complete binding to APTES. Then, coupling agents, namely 1-ethyl-3-(3-dimethylaminopropyl) carbodiimide (EDC) (6.4 mM, 150 μl) (figure 3(d)), and NHS (13 mM, 60 μl) (figure 3(e)), were added to the substrate at 30 min intervals and finally the SARS-CoV-2 mAbs (3 μl, 10 μgml^{-1}) were added to achieve (f) L-SeNPs-mAb conjugate on the biosensor substrate.

2.6. SARS-CoV-2 pseudovirus preparation

This is the preparation of the analyte (SARS-CoV-2 pseudovirus) that will be detected using the LSPR biosensor. The HEK293T cells used in the preparation of the SARS-CoV-2 pseudovirus are adherent cells that were grown and seeded at $5 \times 10_6$ cells in a T-75 flask containing 15 ml of Dulbecco's minimal essential growth medium containing 10% fetal bovine serum (FBS), 0.5% Penicillin-Streptomycin, and incubated for 24 h. before conducting the transfection experiment. When the cell monolayer reached a confluency of about 80%, they were co-transfected with a lentivirus backbone (pNL4.luc encoding the firefly luciferase gene) and a DG614 spike protein (pCDNA3.1) plasmid with a Superfect transfection reagent [35]. The transfected cells were incubated for 48 h before harvesting the pseudovirus-containing culture supernatant. The FBS concentration in the pseudovirus-containing culture supernatant was adjusted to 20%. The supernatant was

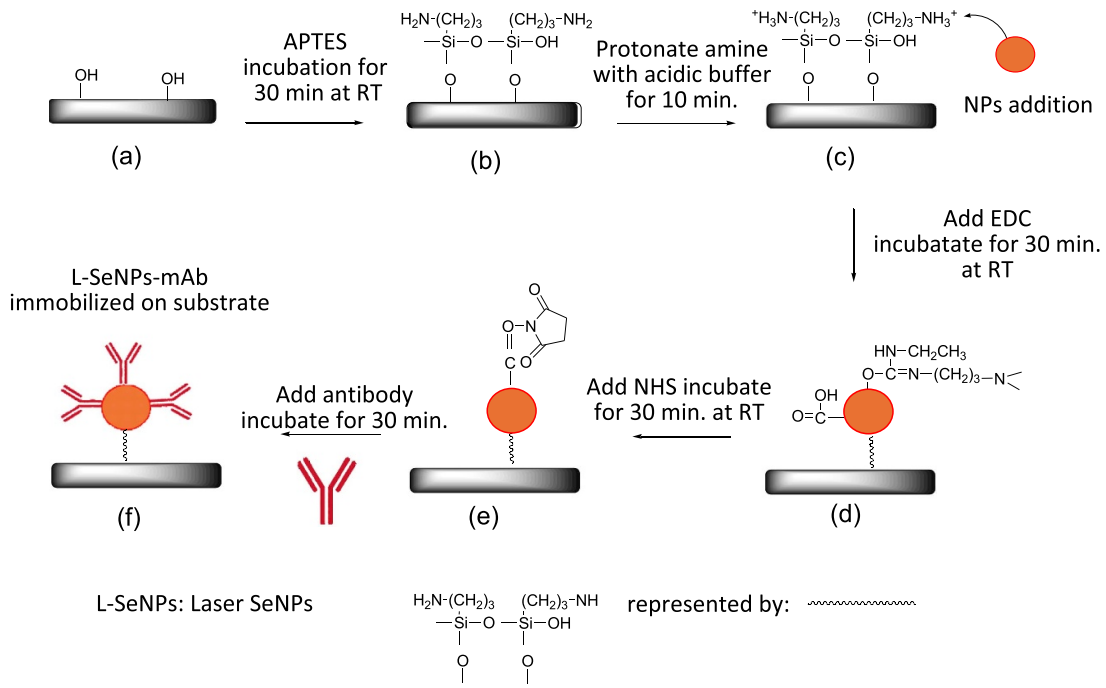

Figure 3. Immobilization of L-SeNPs-mAb conjugate on LSPR sensor: (a) substrate treated with oxygen plasma to form a hydrophilic surface, (b) hydroxyl group functionalized with APTES solution, (c) amine groups were protonated to (NH_3^+) to enable attraction of negatively charged SeNPs, (d) addition of a coupling agent EDC to SeNPs and of (e) NHS coupling agent enables effective and stable bioconjugates with SeNPs, the SARS-CoV-2 mAb is added, resulting in (f) SeNPs-mAb conjugate on a biosensor glass substrate.

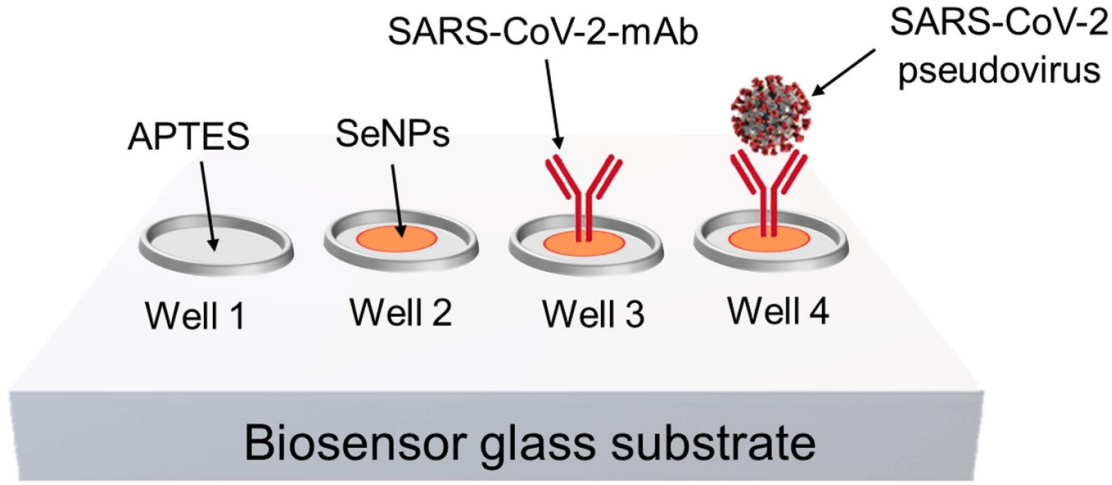

Figure 4. An LSPR biosensing glass substrate pre-coated with APTES (well 1), immobilized with SeNPs (well 2), functionalized with mAb on SeNPs (well 3), and addition of SARS-CoV-2 pseudovirus (well 4).

filtered through a 0.45 μm filter and aliquoted into cryovials for long-term storage at −80 °C until ready for use [36].

2.7. Detection of SARS-CoV-2 pseudovirus using LSPR biosensing substrate

The detection of the SARS-CoV-2 pseudovirus (analyte) was conducted using LSPR. The SARS-CoV-2 pseudovirus generated in section 2.6 at a concentration of 40 μg ml^{-1} was thawed by gently stirring in a water bath heated at 37 °C until all the ice crystals had melted. To attain a final concentration of 10 μgml^{-1}, the analyte was diluted in 1X phosphate-buffered saline (pH 6.0). Wells 1, 2, and 4 were loaded with the analyte (30 μl, at 10 μgml^{-1}), whilst well 3 was loaded with PBS only. The wells were incubated for 10 min at room temperature and washed with 1X PBS (2 × 300 μl). The biosensor substrate (shown in figure 4) was allowed to dry for 10 min under the fume hood and was subjected to LSPR analysis.

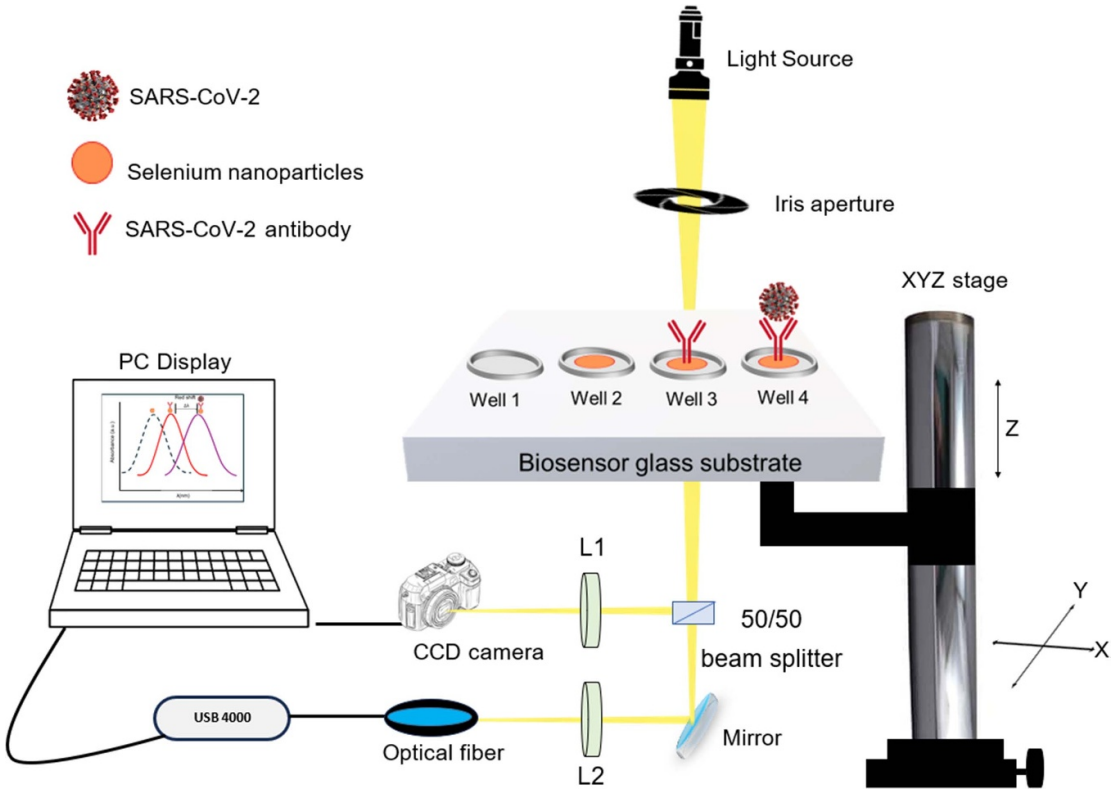

Figure 5. The LSPR biosensing setup comprises 520 nm (1 mW), *XYZ* stage, a CCD camera and computer, a focusing lens (L1 and L2), an optical fiber, and a portable USB spectrometer connected to a computer.

The LSPR setup used in this study is shown in figure 5. The analysis was performed using a transmission spectroscopy setup with a collimated green LED light source at 520 nm and a total power output of 1 mV. The biosensor chip sample was positioned on an *XYZ* sample stage. The transmitted light from the sample was split by a 50/50 beam splitter. One part of the split beam was focused into an optical fiber using a focusing lens, directing the light to a USB 4000 portable spectrometer (Ocean Optics Inc., United States). The other portion of the light was guided to a CCD camera using a reflecting mirror and focusing lens. The CCD camera provided visualization and control of the sample position on the stage. A computer equipped with OceanView and CyberLink Power Director software was used to collect and record the spectra and sample images, respectively. Further data analysis was conducted using OriginPro software.

3. Results and discussion

In this work, SeNPs were synthesized using laser ablation and chemical reduction methods and characterized by UV–vis, DLS, HR-TEM, and Raman spectroscopy. The biosensor chip (glass substrate) was prepared and used to detect SARS-CoV-2 pseudovirus using LSPR.

3.1. Preparation and characterization of SeNPs

Although both chemical reduction and laser ablation techniques can generate small NPs, their advantages and unique characteristics differ. For a sustainable, effective, and economical production of SeNPs, a well-known and eco-friendly top–down Nd:YAG laser ablation method was used in this work [20]. This process involves exposing the selenium pellet immersed in water to radiation for 10 min using a 1064 nm pulsed Nd:YAG laser. The power density of the laser was determined to be $\sim 10^6$ W cm^{-2}, with a 10 ns pulse duration [37]. The successful synthesis of L-SeNPs ablation was confirmed by the visual color change of the solution from colorless to orange. In laser ablation, several factors, including the wavelength, pulse duration, and irradiation time, can influence the size of the NPs produced. Longer wavelengths may result in larger particles due to diminished effective energy absorption and increased thermal effects. At the same time, shorter pulses, such as femtoseconds or picoseconds, typically produce smaller and more homogeneous particles. Additionally, larger particles may result from longer irradiation periods because more material is ablated and has more time to agglomerate.

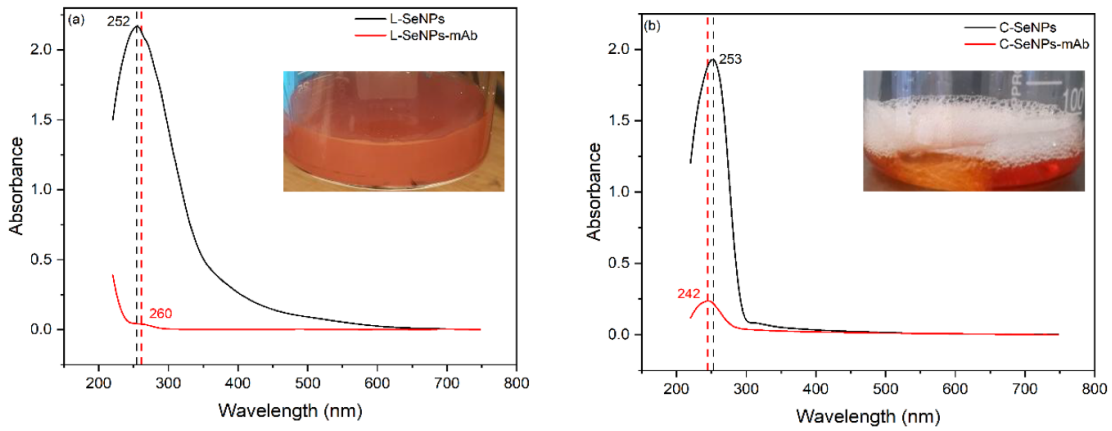

Figure 6. Showing the UV–Vis spectra of SeNPs and SeNPs-mAb conjugate synthesized by (a) laser ablation and (b) chemical reduction methods.

Table 1. The size distribution and surface charges of SeNPs and SeNPs-mAb conjugate.

Samples	DLS sizes (nm ± SD)	PDI	Z potential (mV ± SD)
L-SeNPs	95 ± 13	0.2	−1.53 ± 0.2
L-SeNPs-mAb	130 ± 21	0.3	−30.8 ± 30
C-SeNPs	65 ± 80	0.1	+40 ± 51
C-SeNPs-mAb	118 ± 15	0.2	+22 ± 10

Note: Selenium nanoparticles (SeNPs); Laser SeNPs (L-SeNPs); Laser SeNPs monoclonal antibody (L-SeNPs-mAb); Chemical SeNPs (C-SeNPs); Chemical SeNPs monoclonal antibody (C-SeNPs-mAb).

The C-SeNPs by reducing sodium selenite. This was accomplished by employing ascorbic acid, which served as a reducing agent, along with the stabilizing agent CTAC, which kept the NPs from aggregating and ensured that they remained evenly distributed [16–18]. SeNPs generated by the chemical reduction approach were slightly smaller than those generated by laser ablation; the choice of reducing agent, stabilizer, and reaction conditions possibly influenced the size and homogeneity of the particles.

The UV–Vis absorption spectra of synthesized SeNPs by laser ablation and chemical reduction methods are shown in figure 6. The maximum absorption peaks of SeNPs synthesized by laser ablation and chemical methods were comparable and observed at 252 and 253 nm (figures 6(a) and (b)), respectively [38]. In addition, a decrease in the peak intensities of the SeNPs was observed when the mAb was functionalized on the SeNPs surface. This is due to a change in the electronic environment of the NPs, confirming their attachment to the antibody.

The hydrodynamic size of the NPs, as determined using the DLS, was approximately 95 nm (L-SeNPs) and 65 nm (C-SeNPs). The observed increase in size of L-SeNPs-mAb and C-SeNPs-mAb is attributed to the functionalized mAb on the surface of the SeNPs (see table 1). Moreover, the NPs exhibited a polydispersity index (PDI) of 0.2 (L-SeNPs) and 0.1 (C-SeNPs) before conjugation with antibodies, showing that the NPs were monodispersed. Consequently, the PDI values of the NPs increased after conjugation with antibodies.

The zeta potential analysis revealed that the average potential (mV) of the NPs was −1.53 mV (L-SeNPs) and +40 mV (C-SeNPs). The zeta potential showed that the SeNPs produced by the chemical reduction method have a more positive surface charge due to the presence of CTAC (stabilizer), which conferred a higher density of positively charged functional groups. After conjugation with antibodies, the surface charge of L-SeNPs-mAb was −30.8 mV, whilst that of C-SeNPs-mAb was +22 mV. The reduction in the surface charges of the NPs confirmed the presence of antibodies on the surface of the SeNPs.

The morphology of the synthesized SeNPs was further confirmed using the HR-TEM, which revealed that both SeNPs had a spherical shape (see figures 7(a) and (c)). When the SARS-CoV-2 mAb was functionalized on the SeNPs, the visual effect of the SeNPs-mAb conjugate appeared as dark fringes, which confirmed the presence of mAb on the NP surface.

The synthesized SeNPs were further characterized using Raman spectroscopy for qualitative investigations. In figure 8(a), three prominent peaks were detected beginning with the 247 cm^{-1} shift, which is attributed to the Se–Se stretching mode. The 360 cm^{-1} and 508 cm^{-1} peaks result from Se–O–Se bending and Se–O terminal stretching modes, respectively. These results are consistent with those found in the study of Raman spectra of selenium dioxide at high pressures [39] and in molecular structure of vapor-deposited

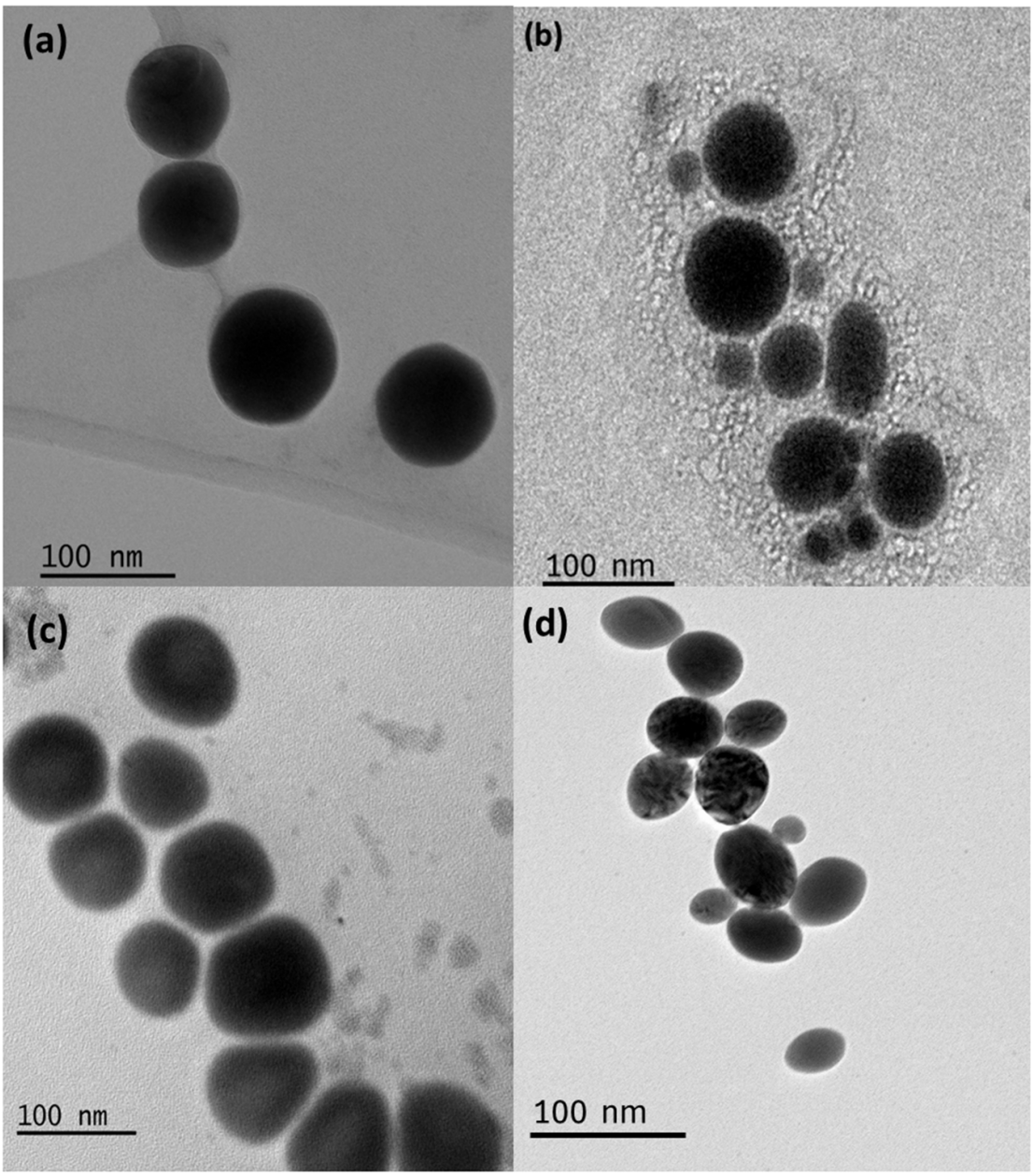

Figure 7. HR-TEM micrograms showing the morphology of (a) L-SeNPs, (b) L-SeNPs-mAb, (c) C-SeNPs, and (d) C-SeNPs-mAb.

amorphous selenium [40]. Figure 8(b) produced a broad Se–Se stretching mode seen on peak 257 cm^{-1}; this change in peak width and peak position (blue-shift) is indicative of increased amorphousity of the SeNPs, expected in chemical bond breakage to form new bonds in a bioconjugation process. Other prominent components of the antibody detected include disulphide bonds at 515 cm^{-1}, tryptophan at 769 $cm^{-1,}$ and a strong peak at 1000 cm^{-1}, which is attributed to the breathing mode of phenylalanine rings present in the protein moiety of antibodies. Similar results were obtained by Rumaling *et al* [41] in the study of Biofingerprint detection of coronavirus using Raman spectroscopy [41].

A Raman spectroscopy assessment of SeNPs synthesized using the chemical method was conducted similarly to the laser ablation method. In figure 9(a), a strong peak from Se–Se bonds is seen at 249 cm^{-1} followed by the Se–O–Se bending (375 cm^{-1}) and Se–O terminal modes (507 cm^{-1}), similar to the laser method, confirming the formation of SeNPs using chemical methods. The low signals observed on the rest of the spectrum arise from the aliphatic chains of the starting material CTAC and the carbon-oxygen bonds of ascorbic acid. For figure 9(b), the Se–Se bond at 249 cm^{-1} has reduced intensity probably due to bioconjugation, while a new peak was detected at 288 $cm^{-1,}$ which belongs to the Se–Se bond. The difference in peak position can be explained by the increased intermolecular forces from the reagents, which lead to deformation of the Se–Se bond [41, 42]. The prominence of this peak could be used to confirm

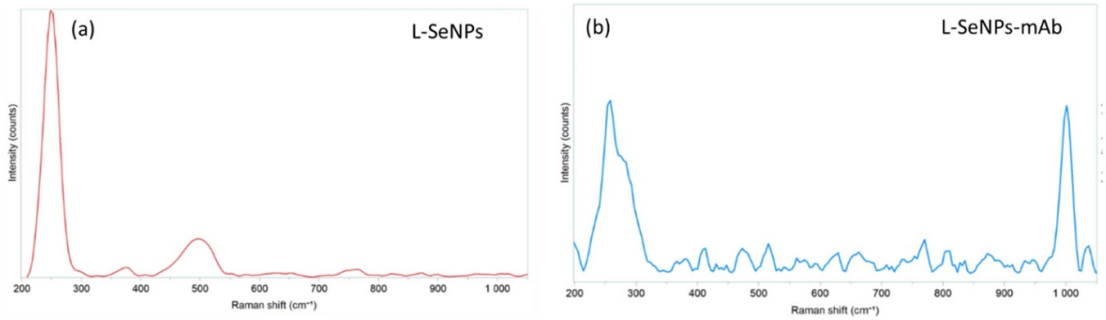

Figure 8. Raman spectra of (a) L-SeNPs, and (b) L-SeNPs-mAb.

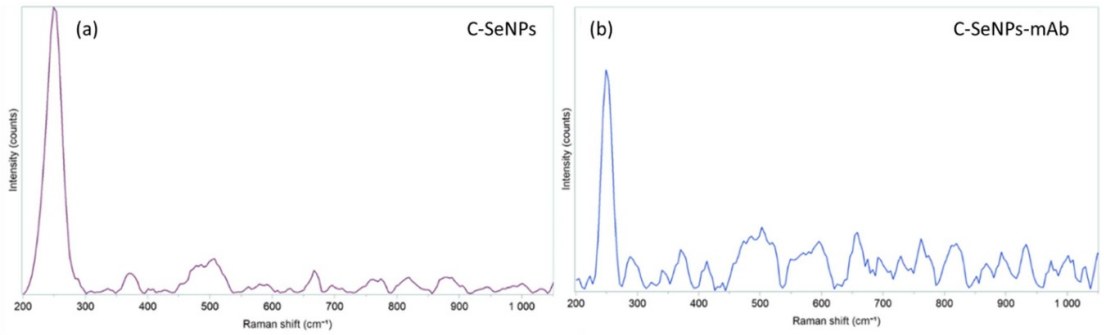

Figure 9. Raman spectra of (a) C-SeNPs, and (b) C-SeNPs-mAb.

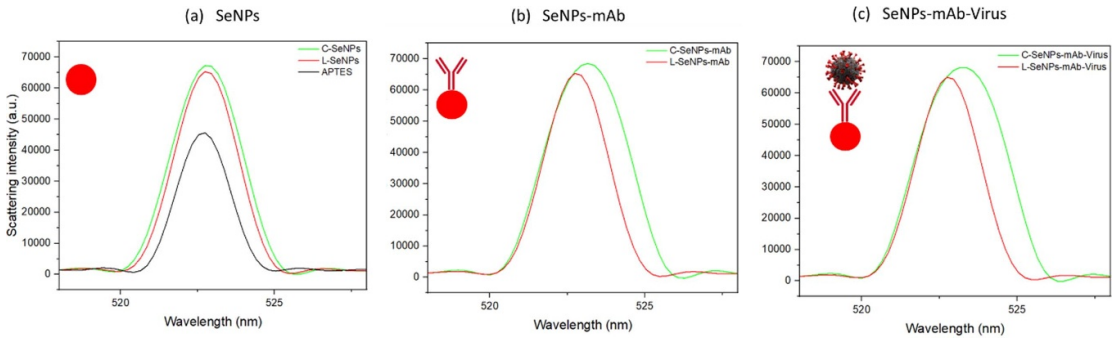

Figure 10. Comparison of the scattering intensities of APTES (negative control) to laser-ablated and chemical synthesized (a) SeNPs, (b) SeNPs-mAb conjugate, and (c) SeNPs-mAb-virus conjugate.

bioconjugation since it is absent in figure 9(a). Secondly, amino acids tryptophan and tyrosine emerged in the 600–700 cm^{-1} region. Low-intensity peaks from amino acid side chains were detected in the 700–1000 cm^{-1} region, with the absence of phenylalanine as seen in figures 9(b), and a similar pattern of results was obtained by Sato *et al* [43].

3.2. Detection of SARS-CoV-2 using LSPR biosensing

To detect the SARS-CoV-2 pseudovirus and to examine how the scattering signals of SeNPs and SeNPs-mAb conjugate contribute to the LSPR effect, the prepared biosensing glass substrate (see figure 4) was used. The scattering intensity measurements and wavelength shifts for the samples are shown in figure 10.

The scattering intensities of the SeNPs produced by the laser ablation and chemical reduction methods were comparable and stronger than that of a negative control sample (APTES), and both SeNPs exhibited a redshift (see figure 10(a)). The results support the findings of Wang and Cao [44] that NPs scatter light more effectively than dielectric materials like glass [44]. In this study, the dielectric material used was a glass substrate coated with APTES. It was anticipated that the small-sized chemical SeNPs would scatter light more intensely than the slightly bigger L-SeNPs, since the scattering efficiency of NPs is proportional to the square

of their volume. However, this phenomenon was not observed; only a small variation in the NPs' scattering intensity and wavelength shift was observed between the SeNPs (figure 10(a)). One possible explanation for the slight variation could be that both SeNPs were spherical and had relatively similar diameters.

When the SARS-CoV-2 mAb was functionalized to SeNPs, the LSPR scattering intensity spectrum revealed that both SeNPs exhibited a redshift (figure 10(b)). The C-SeNPs reduction method showed a slightly higher redshifted LSPR peak at $\lambda = 522.7332$ nm than the laser SeNPs ($\lambda = 522.7027$ nm). This difference could be due to the differences in surface chemistry between mAb and the two SeNPs. The wavelength (λ) redshift observation confirmed the successful functionalization of mAb to SeNPs. The spectrum in figure 10(c) showed that the C-SeNPs LSPR peak shifted to a longer wavelength ($\lambda = 523.1481$ nm) compared to the L-SeNPs LSPR peak ($\lambda = 522.7765$ nm) when the antibody captured the SARS-CoV-2 antigen. The observed change in peak intensities or a change in the local RI near the NP surface could be due to the specific binding between the analyte and the antibody.

The comparative analysis between the two types of SeNPs was conducted to assess how their synthetic origin impacts their plasmonic response and biosensing characteristics. The difference in LSPR shifts between the two types of NPs reflects their sensitivity to biomolecular interactions. The overall findings of this study demonstrate that, in comparison to L-SeNPs, the LSPR peak for C-SeNPs reduction approach exhibited a slight redshift (longer wavelength), indicating that these NPs are good candidates for biosensing applications in optical techniques. Typically, the chemical reduction method frequently yields consistent NP morphology and a stable surface that inhibits aggregation because of the type of stabilizing agent employed; this leads to strong and distinct LSPR characteristics [45]. Whereas NPs produced by lasers are more likely to aggregate, because they are synthesized entirely of pure water; there are no stabilizers or surfactants employed, and this may result in weaker and less consistent plasmonic reactions [19].

The results of this investigation correspond with those described in previous studies. For instance, it was reported by Hollis [46] that increased light absorption and scattering can be used to detect environmental changes, including pathogen binding, when light interacts with MNPs in LSPR [46]. In a related study, Wang *et al* [47], developed a new gold nanorods (GNRs) biosensor based on LSPR to detect the hepatitis B surface antigen (HBsAg), an indicator of active hepatitis B virus replication. mAbs against the antigen were used and functionalized on the GNRs. The results of the investigation showed that the LSPR biosensor based on GNRs could detect HBsAg, with a limit of detection (LOD) of 0.01 IU ml^{-1} [47]. Furthermore, using LSPR immunosensors, Basso *et al* [48] proposed a method for early dengue virus detection. The authors used gold NPs (AuNPs) as signal enhancers, which were functionalized with antibodies specific to the dengue virus. The antigen detection by the LSPR sensor was based on the LSPR wavelength shift observed after functionalization with antibodies and subsequent exposure to the dengue antigen [48].

4. Conclusion

In this study, SeNPs were synthesized via two distinct methods, and their scattering intensities in LSPR measurements were compared. The wavelength shifts induced by the SeNPs were analyzed, and the performance of the LSPR optical biosensor for detecting SARS-CoV-2 pseudovirus was evaluated. C-SeNPs exhibited a slightly greater impact on the LSPR response than L-SeNPs. These findings suggest that C-SeNPs are suitable for incorporation into LSPR biosensors for SARS-CoV-2 pseudovirus detection. These results highlight the potential to tune the LSPR properties of SeNPs through controlled synthesis, enabling their application in biosensing. Future work will further assess C-SeNPs for LSPR-based detection, focusing on sensitivity, specificity, and LOD. Once validated, the technique will be translated into a cost-effective, yet robust, POC diagnostic platform designed for application in resource-limited settings.

Data availability statement

All data that support the findings of this study are included within the article (and any supplementary files).

Acknowledgments

For financial support, the authors would like to acknowledge the Department of Science and Innovation (DSI), the National Research Foundation (NRF), the Council for Scientific and Industrial Research (CSIR), and the University of Cape Town (Department of Chemical Engineering) for supporting this research.

Conflict of interest

The authors declare no financial or commercial conflict of interest.

Author contributions

Z K S Mcotshana 0000-0002-5814-1311
Conceptualization (lead), Data curation (lead), Methodology (lead), Writing – original draft (lead), Writing – review & editing (lead)

L N Thwala 0000-0002-0687-3908
Conceptualization (equal), Supervision (lead), Writing – review & editing (equal)

S Ombinda-Lemboumba
Data curation (supporting), Writing – review & editing (supporting)

R Ramokolo
Methodology (supporting)

M Sekhwama
Data curation (supporting), Writing – review & editing (supporting)

S L Thobakgale 0000-0003-2491-6948
Data curation (supporting), Writing – review & editing (supporting)

M Y Lugongolo
Data curation (supporting), Writing – review & editing (supporting)

L Hlekelele 0000-0003-0443-3578
Data curation (supporting), Writing – review & editing (supporting)

K T Mpofu 0000-0001-8986-2253
Data curation (supporting), Writing – review & editing (supporting)

E Van Steen 0000-0003-4659-8522
Supervision (lead), Writing – review & editing (equal)

P Mthunzi-Kufa
Conceptualization (supporting), Supervision (lead), Writing – review & editing (supporting)

References

[1] Arranz A and Ripoll J 2015 Advances in optical imaging for pharmacological studies *Front. Pharmacol.* **6** 1–7
[2] Yang H, Zhao C, Li R, Shen C, Cai X, Sun L, Luo C and Yin Y 2018 Noninvasive and prospective diagnosis of coronary heart disease with urine using surface-enhanced Raman spectroscopy *Analyst* **143** 2235–42
[3] Sufiawati I, Harmiyati R, Nur'aeny N, Indrati A R, Lesmana R, Wisaksana R and Amalia R 2023 Detection of human herpesviruses in sera and saliva of asymptomatic HIV-infected individuals using multiplex RT-PCR DNA microarray *Pathogens* **12** 993
[4] Liu Y *et al* 2023 Nano-biosensor for SARS-CoV-2/COVID-19 detection: methods, mechanism and interface design *RSC Adv.* **13** 17883–906
[5] Lamb L E L *et al* 2020 Rapid detection of novel coronavirus/severe acute respiratory syndrome coronavirus 2 mediated isothermal amplification *PloS One* **2** 1–15
[6] Maddali H, Miles C E, Kohn J and O'Carroll D M 2021 Optical biosensors for virus detection: prospects for SARS-CoV-2/COVID-19 *ChemBioChem* **22** 1176–89
[7] Behera S, Rana G, Satapathy S, Mohanty M, Pradhan S, Panda M K, Ningthoujam R, Hazarika B N and Singh Y D 2020 Biosensors in diagnosing COVID-19 and recent development *Sens. Int.* **1** 100054
[8] Huang C-L, Ji Huang H, Chen S-H, Huang Y-S, Kao P-C, Chou Chau Y-F and Chiang H-P 2021 Localized surface plasmon resonance enhanced by the light-scattering property of silver nanoparticles for improved luminescence of polymer light-emitting diodes *J. Ind. Eng. Chem.* **103** 283–91
[9] Philip A and Kumar A R 2022 The performance enhancement of surface plasmon resonance optical sensors using nanomaterials: a review *Coord. Chem. Rev.* **458** 214424
[10] Lin H T H, Yang C-K, Lin C-C, Wu A M H, Wang L A and Huang N-T 2017 A large-area nanoplasmonic sensor fabricated by rapid thermal annealing treatment for label-free and multi-point immunoglobulin sensing *Nanomaterials* **7** 100
[11] Maier S A and Atwater H A 2005 Plasmonics: localization and guiding of electromagnetic energy in metal/dielectric structures *J. Appl. Phys.* **98** 011101
[12] Fahimi-Kashani N, Orouji A, Ghamsari M, Sahoo S K and Hormozi-Nezhad M R 2023 *Plasmonic Noble Metal (Ag and Au) Nanoparticles: From Basics to Colorimetric Sensing Applications* (Elsevier Inc) (https://doi.org/10.1016/B978-0-323-99454-5.00005-6)
[13] Jain P K, Lee K S, El-Sayed I H and El-Sayed M A 2006 Calculated absorption and scattering properties of gold nanoparticles of different size, shape, and composition: applications in biological imaging and biomedicine *J. Phys. Chem. B* **110** 7238–48
[14] Connor E E, Mwamuka J, Gole A, Murphy C J and Wyatt M D 2005 Gold nanoparticles are taken up by human cells but do not cause acute cytotoxicity *Small* **1** 325–7
[15] Kumar S, Aaron J and Sokolov K 2008 Directional conjugation of antibodies to nanoparticles for synthesis of multiplexed optical contrast agents with both delivery and targeting moieties *Nat. Protoc.* **3** 314–20

[16] Hassan R M, Elsayed M, Kholief T E, Hassanen N H M, Gafer J A and Attia Y A 2021 Mitigating effect of single or combined administration of nanoparticles of zinc oxide, chromium oxide, and selenium on genotoxicity and metabolic insult in fructose/streptozotocin diabetic rat model *Environ. Sci. Pollut. Res.* **28** 48517–34
[17] Xu X, Pan Y, Liu X, Han Z and Chen S 2023 Constructing selenium nanoparticles with enhanced storage stability and antioxidant activities via conformational transition of curdlan *Foods* **12** 563
[18] Baig N, Kammakakam I, Falath W and Kammakakam I 2021 Nanomaterials: a review of synthesis methods, properties, recent progress, and challenges *Mater. Adv.* **2** 1821–71
[19] Malik S, Singh J, Goyat R, Saharan Y, Chaudhry V, Umar A, Ibrahim A A, Akbar S, Ameen S and Baskoutas S 2023 Nanomaterials-based biosensor and their applications: a review *Heliyon* **9** e19929
[20] Kh N, Neean A, Arkan F M, Buraihi K and Ali S H 2024 Optical nanoparticle synthesis : a comprehensive laser ablation review *Front. Oncol.* **13** 1183766
[21] Kalaparthi R *et al* 2020 Synthesis of selenium nanoparticles using sodium Selenite [Se(IV)] as A precursor and titanium(III) chloride as a reducing agent *Int. J. Eng. Res.* **V9** 359–60
[22] Manoto S L, El-Hussein A, Malabi R, Thobakgale L, Ombinda-Lemboumba S, Attia Y A, Kasem M A and Mthunzi-Kufa P 2021 Exploring optical spectroscopic techniques and nanomaterials for virus detection *Saudi J. Biol. Sci.* **28** 78–89
[23] Chaudhary S, Umar A and Mehta S K 2014 Surface functionalized selenium nanoparticles for biomedical applications *J. Biomed. Nanotechnol.* **10** 3004–42
[24] Samynathan R, Venkidasamy B, Ramya K, Muthuramalingam P, Shin H, Kumari P S, Thangavel S and Sivanesan I 2023 A recent update on the impact of nano-selenium on plant growth, metabolism, and stress tolerance *Plants* **12** 1–24
[25] Mostafavi E, Medina-Cruz D, Truong L B, Kaushik A and Iravani S 2022 Selenium-based nanomaterials for biosensing applications *Mater. Adv.* **3** 7742–56
[26] Deepa T, Mohan S and Manimaran P 2022 A crucial role of selenium nanoparticles for future perspectives *Results Chem.* **4** 100367
[27] Huang X, Zhu Y and Kianfar E 2021 Nano biosensors: properties, applications and electrochemical techniques *J. Mater. Res. Technol.* **12** 1649–72
[28] Kunwar S, Pandit S, Jeong J-H and Lee J 2020 Improved photoresponse of UV photodetectors by the incorporation of plasmonic nanoparticles on GaN through the resonant coupling of localized surface plasmon resonance *Nano-Micro Lett.* **12** 1–16
[29] Bigdeli A, Ghasemi F, Golmohammadi H, Abbasi-Moayed S, Nejad M A F, Fahimi-Kashani N, Jafarinejad S, Shahrajabian M and Hormozi-Nezhad M R 2017 Nanoparticle-based optical sensor arrays *Nanoscale* **9** 16546–63
[30] Li A, Isaacs S, Abdulhalim I and Li S 2015 Ultrahigh enhancement of electromagnetic fields by exciting localized with extended surface plasmons *J. Phys. Chem. C* **119** 19382–9
[31] Stewart M E, Anderton C R, Thompson L B, Maria J, Gray S K, Rogers J A and Nuzzo R G 2008 Nanostructured plasmonic sensors *Chem. Rev.* **108** 494–521
[32] Anker J N, Hall W P, Lyandres O, Shah N C, Zhao J and Van Duyne R P 2009 Biosensing with plasmonic nanosensors *Nanosci. Technol. A Collect. Rev. Nat. J.* **7** 308–19
[33] Du H, Castaing V, Guo D and Viana B 2020 Rare-earths doped-nanoparticles prepared by pulsed laser ablation in liquids *Ceram. Int.* **46** 26299–308
[34] Mina B M J and Andersen K G 2021 COVID-19 testing: one size does not fit all *Science* **37** 126–8
[35] Wibmer C K *et al* 2021 SARS-CoV-2 501Y.V2 escapes neutralization by South African COVID-19 donor plasma *Nat. Med.* **27** 622–5
[36] Sarzotti-Kelsoe M *et al* 2014 Optimization and validation of the TZM-bl assay for standardized assessments of neutralizing antibodies against HIV-1 *J. Immunol. Methods* **409** 131–46
[37] Naser H, Shanshool H M and Imhan K I 2021 Parameters affecting the size of gold nanoparticles prepared by pulsed laser ablation in liquid *Braz. J. Phys.* **51** 878–98
[38] Harish V, Ansari M M, Tewari D, Gaur M, Yadav A B, García-Betancourt M-L, Abdel-Haleem F M, Bechelany M and Barhoum A 2022 Nanoparticle and nanostructure synthesis and controlled growth methods *Nanomaterials* **12** 1–30
[39] Stanila D, Smith W and Anderson A 2000 Raman spectra of selenium dioxide at high pressures *Spectrosc. Lett.* **33** 555–67
[40] Goldan A H, Li C, Pennycook S J, Schneider J, Blom A and Zhao W 2016 Molecular structure of vapor-deposited amorphous selenium *J. Appl. Phys.* **120** 135101
[41] Rumaling M I, Chee F P, Bade A, Goh L P W and Juhim F 2023 Biofingerprint detection of corona virus using Raman spectroscopy: a novel approach *SN Appl. Sci.* **5** 197
[42] Jackson N, Hassan J and Byrne H J 2023 Raman spectroscopic analysis of human serum samples of convalescing COVID-19 positive patients *Clin. Spectrosc.* **5** 100028
[43] Sato Y, Nagatoishi S, Noguchi S and Tsumoto K 2023 Raman spectroscopic analysis of highly-concentrated antibodies under the acid-treated conditions *Pharma Res.* **40** 1853–64
[44] Wang X and Cao Y 2020 Characterizations of absorption, scattering, and transmission of typical nanoparticles and their suspensions *J. Ind. Eng. Chem.* **82** 324–32
[45] Liang H, Wei H, Pan D and Xu H 2015 Chemically synthesized noble metal nanostructures for plasmonics *Nanotechnol. Rev.* **4** 289–302
[46] Hollis J 2024 Plasmonic nanomaterials for sensing and detection of pathogens *J. Nanomed. Nanotechnol.* **15** 10–12
[47] Wang X, Li Y, Wang H, Fu Q, Peng J, Wang Y, Du J, Zhou Y and Zhan L 2010 Gold nanorod-based localized surface plasmon resonance biosensor for sensitive detection of hepatitis B virus in buffer, blood serum and plasma *Biosens. Bioelectron.* **26** 404–10
[48] Basso C R, Tozato C C, Crulhas B P, Castro G R, Junior J P A and Pedrosa V A 2018 An easy way to detect dengue virus using nanoparticle-antibody conjugates *Virology* **513** 85–90